ACS OMEGA

Open Access

http://pubs.acs.org/journal/acsodf

Article

Engineering of CuMOF-SWCNTs@AuNPs-Based Electrochemical Sensors for Ultrasensitive and Selective Monitoring of Imatinib in Human Serum

Xuanming Xu, Wei Li, Hao Xin, Lian Tang, Xiaoyan Zhou, Tingting Zhou, Chao Xuan, Qingwu Tian, and Deng Pan*

Cite This: *ACS Omega* 2024, 9, 4744−4753

Read Online

ACCESS | Metrics & More | Article Recommendations | Supporting Information

ABSTRACT: Imatinib (IMA) is a common chemotherapy drug for the treatment of leukemia and can potentially lead to drug resistance and toxicity during the course of treatment. Monitoring IMA concentrations in body fluids is necessary to optimize therapeutic schedules and avoid overdosage. In this paper, a novel ultrasensitive electrochemical sensor based on CuMOF and SWCNTs@AuNPs was developed to determine this antileukemic drug. Herein, AuNPs were supported on carboxylic single-walled carbon nanotubes (SWCNT-COOH), and then poly(diallyldimethylammonium chloride) (PDDA) was used as a dispersant to overcome the internal van der Waals interactions among the CNTs, further increasing the AuNP loading. Moreover, the morphology, structure, composition, and electrochemical properties of the CuMOF-SWCNTs@AuNPs composite film were characterized using SEM, TEM, FT-IR, UV−vis, XRD, XPS, CV, and EIS. Due to the advantage of the superior electrocatalytic and conductive properties of SWCNTs@AuNPs and their preferable adsorptivity and affinity to IMA of CuMOF, the fabricated glassy carbon electrode significantly improved the determination performance via their synergetic amplified effect. Under optimal conditions, a wide linear response was exhibited in the range from 0.05 to 20.0 μM and the low detection limit of 5.2 nM. In addition, our prepared sensor has been applied to the analysis of IMA in blood serum samples with acceptable results. Therefore, our CuMOF-SWCNTs@AuNPs-based electrochemical sensor possessed prominent sensing responses for IMA, which could be used as a prospective approach in clinical application.

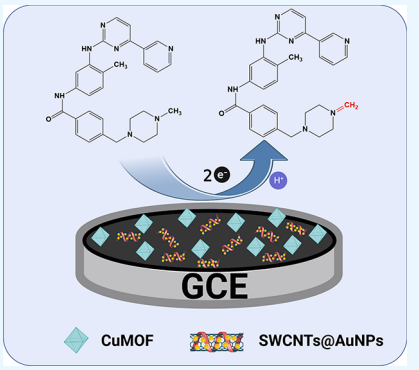

1. INTRODUCTION

Imatinib (IMA, Gleevec) is a category of dihydrophenylaminopyrimidine derivative that targets BCR-ABL kinase. As a tyrosine kinase inhibitor (TKI), this drug is widely applied to treat chronic myelogenous leukemia (CML), as well as gastrointestinal stromal tumors (GISTs), owing to its inhibitory effect on the c-Kit receptor.[1,2] In clinical applications, various drug reactions and survival rates of patients have been confirmed to be associated with different IMA concentrations in plasma.[3−5] Moreover, IMA frequently induces large interindividual but low intraindividual pharmacokinetic variability in clinical drug usage.[6] Thus, according to these situations, the detection of the concentrations of IMA needs an extremely sensitive method to assess the risk of chemotherapy patients aiming to obtain a good curative effect.

To date, different analytical technologies for IMA detection, including high-performance liquid chromatography (HPLC),[7] ultraviolet spectroscopy,[8] surface-enhanced Raman spectroscopy (SERS),[9] and fluorescence sensors,[10] have been used. However, most of these methods are not suitable for large-scale applications due to their toxic solvents, time-consuming nature, or high implementation costs. Conversely, electrochemical sensors with advantages in terms of detection efficiency, usage convenience, and high sensitivity[11,12] have attracted growing attention in pharmaceutical analysis;[13,14] these methods provide a fast and relatively inexpensive analytical platform for therapeutic drug monitoring (TDM) in real biological samples.

Metal−organic frameworks (MOFs), as three-dimensional orderly coordination polymers, are self-assembled by inorganic metal clusters and/or ion nodes and organic ligand bridges. In view of their advantages, such as the larger specific surface area, tunable porosity, and abundant active sites, MOFs are perceived as desirable nanomaterials in the fields of adsorption, drug delivery, and energy storage.[15,16] As a classic square-hole MOF, CuMOF [$Cu_3(BTC)_2$, HKUST-1] possesses prominent adsorption and catalysis capability, and its activated empty phase has satisfactory affinity for IMA via hydrogen bonds.[17,18]

Received: October 13, 2023
Revised: December 21, 2023
Accepted: December 27, 2023
Published: January 20, 2024

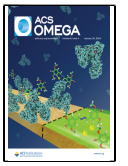

Scheme 1. Schematic of a Simple Electrochemical Sensor Based on CuMOF-SWCNTs@AuNPs for Detecting IMA in Human Blood Serum

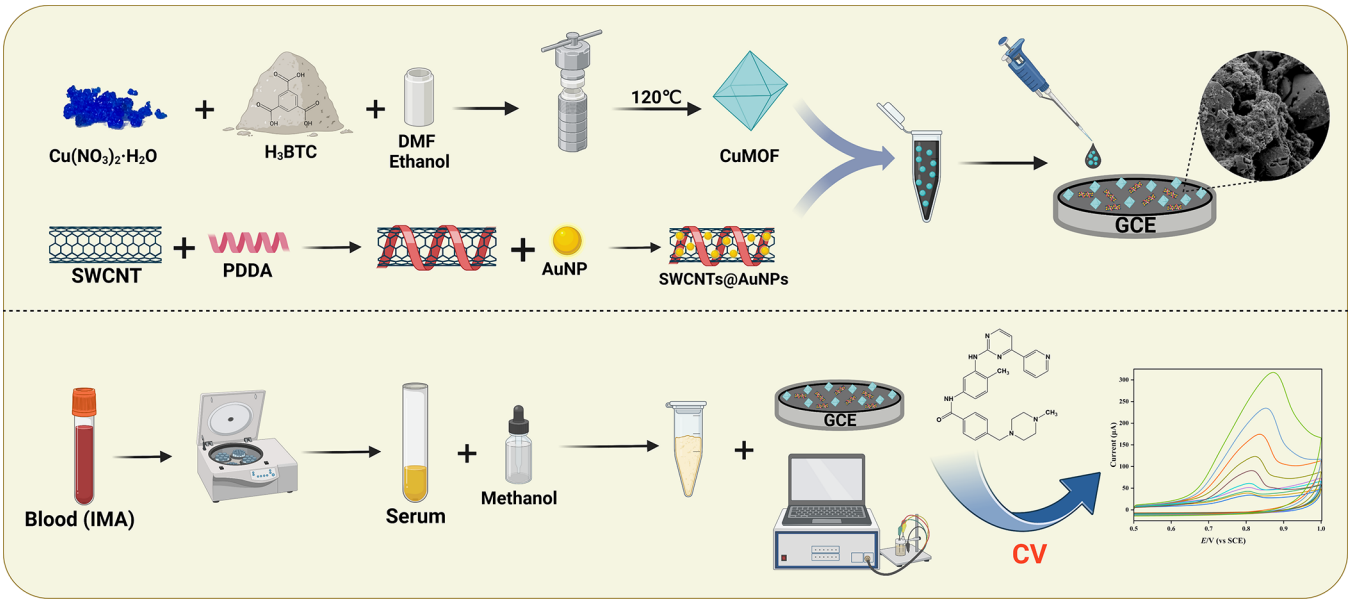

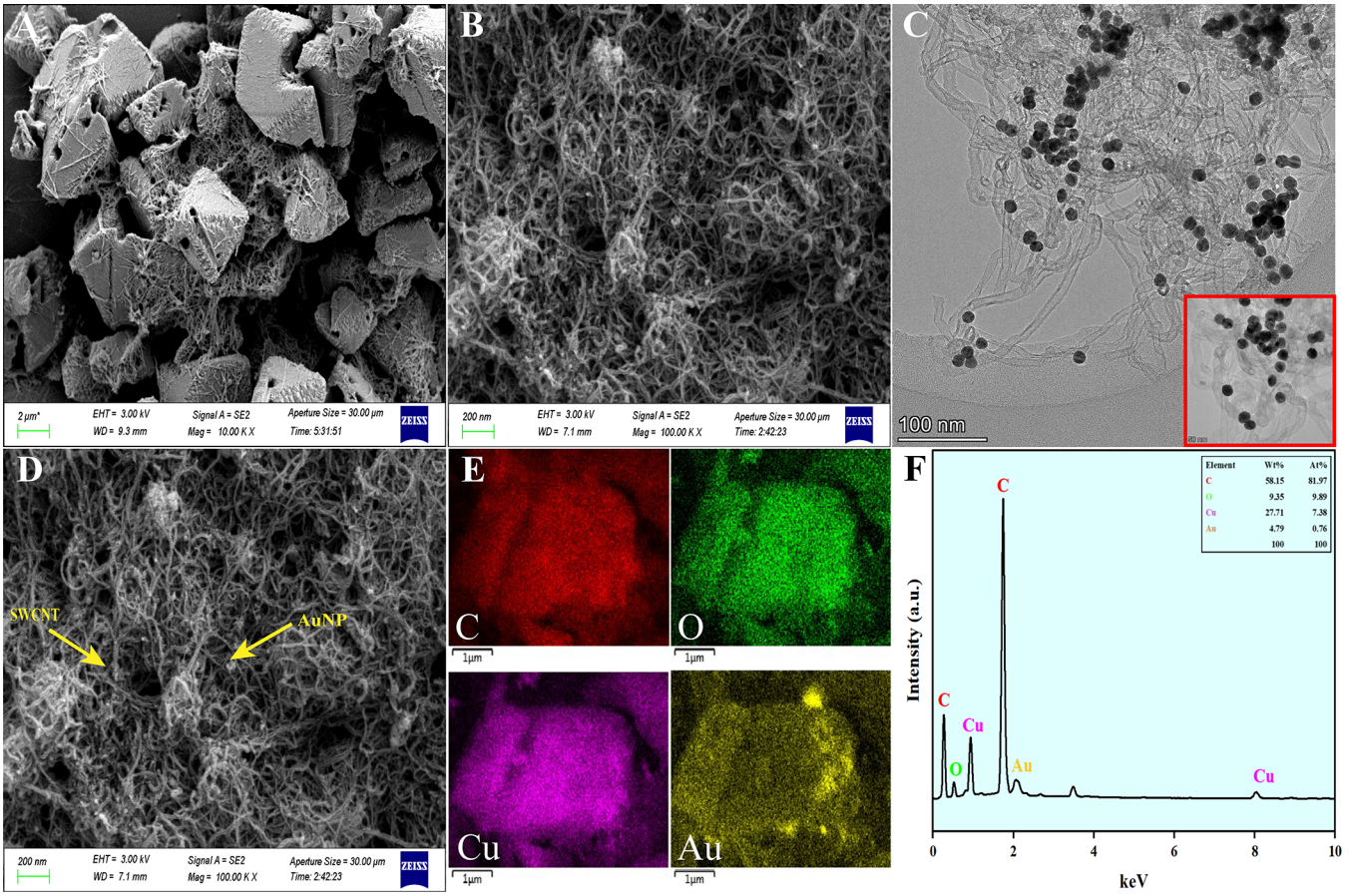

Figure 1. SEM images of CuMOF (A) and SWCNT-COOH (B). TEM image of SWCNTs@AuNPs (C) (inset shows high magnification). SEM (D) and EDS mapping (E,F) images of CuMOF-SWCNTs@AuNPs.

However, most MOFs have inherently poor ionic conductivity and stability in aqueous media, limiting the progression of electrochemical catalysis. To address this problem, a viable approach that merges MOF materials with excellent conductive materials has been developed.

In recent studies, various types of nanomaterials, such as carbon nanotubes (CNTs) and metallic material-based composites, have been increasingly used in sensors.[19−21] CNTs have been regarded as promising materials for applications in the electrochemistry field owing to their large

https://doi.org/10.1021/acsomega.3c08002
ACS Omega 2024, 9, 4744−4753

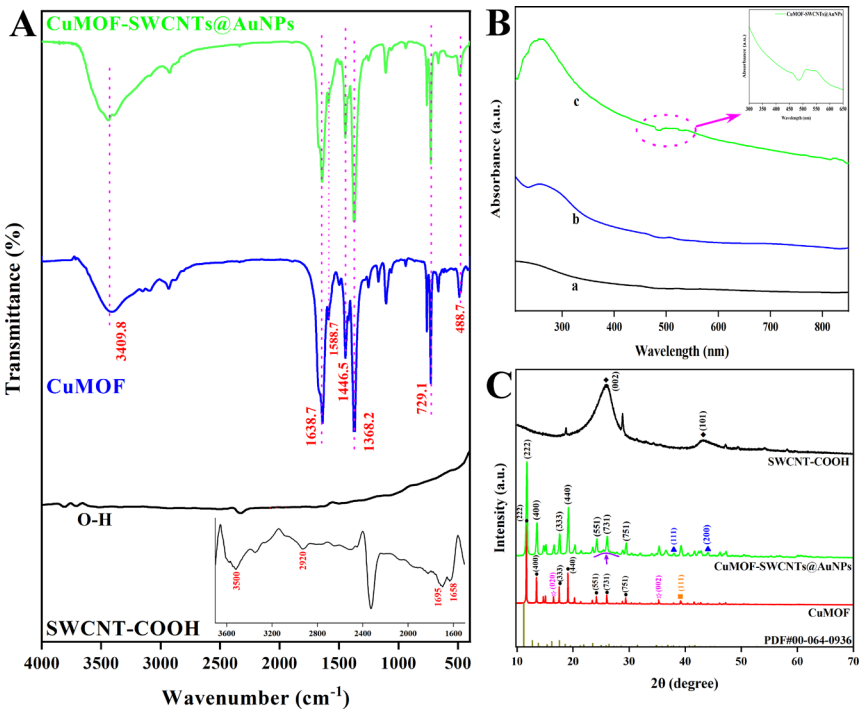

Figure 2. FT-IR spectra (A) of SWCNT-COOH (inset shows the spectra with baseline correction), CuMOF, and CuMOF-SWCNTs@AuNPs. UV−vis spectra (B) and XRD patterns (C) of SWCNT-COOH, CuMOF, and CuMOF-SWCNTs@AuNPs.

graphitic degree and unique channel structure. In particular, carboxylated single-walled carbon nanotubes (SWCNT-COOH) are rolled-up single layers of graphite with a high surface area, desirable electrical conductivity, and preferable solubility[22] and have become good candidates as support materials to improve electrochemical sensing performance.

Gold nanoparticles (AuNPs) are promising materials for electrochemical detection due to their strong electrical conductivity and catalytic properties. In addition, AuNPs could also be synthesized and conjugated with various functionalized agents, including polymers, aptamers, and CNTs. Additionally, AuNPs normally tend to aggregate due to interparticle interactions with high surface energies and van der Waals forces, which decrease the catalytic activity.[23] Thus, composite structures based on the synergistic combination of carbon materials and AuNPs have been widely studied as alternative systems for the determination of sulfite,[19] hydrazine,[24] dicapthon pesticide,[25] and glucose.[26] Although CNT@AuNP nanostructures exhibit superior electroactivity, their insufficient ability to adsorb drugs leads to a decrease in their detection sensitivity.

To the best of our knowledge, the utilization of a CuMOF-based method for IMA determination has rarely been reported. Herein, positively charged poly(diallyldimethylammonium chloride) (PDDA) was used as a cross-linking agent to overcome the inherent van der Waals forces among pristine SWCNTs and further increase the loading ability of AuNPs. Moreover, CuMOF in this assay had several advantages, such as regular shape, facile modification, and simple synthesis procedure. An innovative and convenient strategy was developed (as shown in Scheme 1) by fabricating a sensor consisting of a combination of CuMOF with SWCNTs@AuNPs. Based on the unique, distinctive, and complementary properties of both modified materials at the electrode, they were used to enhance the figure of merits of the sensor, which widened the electrochemical applications of MOFs and expanded the quantifiable determination approaches of antineoplastic drugs. All results indicated that the designed method was successfully prepared for IMA detection.

2. EXPERIMENTAL SECTION

Chemicals, reagents, and apparatus; synthesis of CuMOF, SWCNT-PDDA, and SWCNTs@AuNPs; fabrication of CuMOF-SWCNTs@AuNPs/GCE; processing procedures; and detection of the IMA sample are provided in the Supporting Information in detail.

3. RESULTS AND DISCUSSION

3.1. Characterization of CuMOF-SWCNTs@AuNPs. To enhance the performance of the electrochemical sensor, CuMOF and SWCNTs@AuNPs nanohybrids showing high adsorptivity and conductivity were chosen as the substrate materials to modify the GCE. The successful fabrication of CuMOF and SWCNTs@AuNPs nanohybrids was initially determined via SEM and TEM. As indicated in Figure 1A, the dispersed CuMOF crystals had a well-defined octahedral geometry with regular edges and a relatively uniform particle size. In Figure 1B, long and classical striplike SWCNTs formed a homogeneous hybridized material, coexisting with some wrapped structure. The TEM image (Figure 1C) shows that the SWCNT supports were decorated by spherical gold nanostructures with relatively uniform sizes. These results were potentially ascribed to the interaction of different charges between the PDDA-capped SWCNTs and AuNPs. From Figure 1D, the SWCNTs@AuNPs were heterogeneously dispersed over the cubic layered surface of the CuMOF framework, which could be caused by weak $\pi-\pi$ stacking at the interface, following a parallel arrangement. Finally, SEM−EDS mapping images (Figure 1E) and energy-dispersive X-ray (EDX) analysis (Figure 1F) confirmed that hybrid crystals of

https://doi.org/10.1021/acsomega.3c08002
ACS Omega 2024, 9, 4744−4753

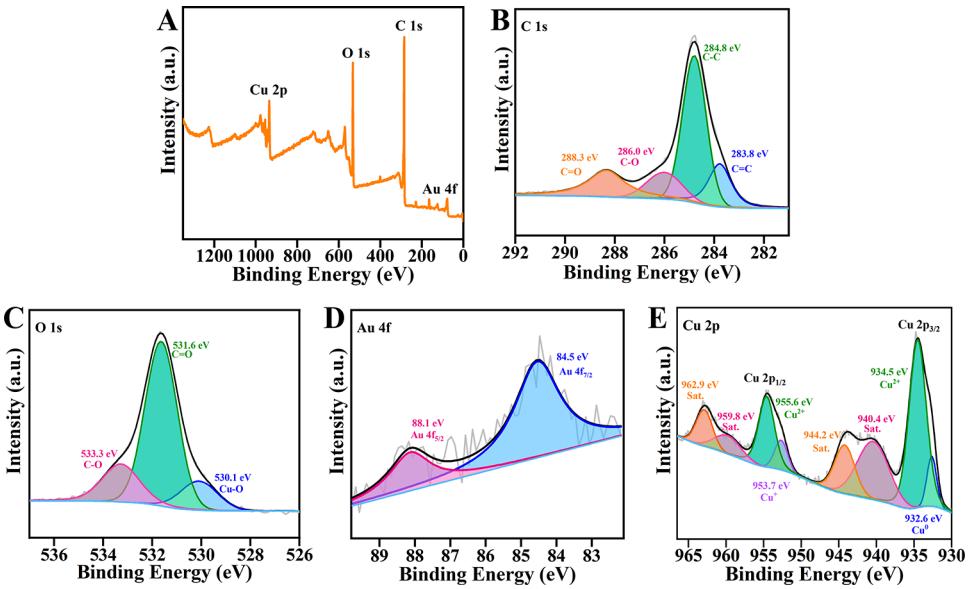

Figure 3. Full-scale XPS spectra (A) of CuMOF-SWCNTs@AuNPs. High-resolution XPS spectra of C 1s (B), O 1s (C), Au 4f (D), and Cu 2p (E).

CuMOF-SWCNTs@AuNPs consisted of the main corresponding elements (C, O, Cu, and Au).

Fourier transform infrared spectrometry (FT-IR) was used to illustrate the surface molecular structure and chemical bonds. For pure SWCNT-COOH (Figure 2A and inset), the bands at 1658 and 1695 cm^{-1} were attributed to C═C and C═O stretching from the inherent structure. In addition, the C−H and O−H peaks were shown at 2920 and 3500 cm^{-1}, respectively,[27,28] and the introduction of carboxyl groups (−COOH) could improve the hydrophilicity and stability of the SWCNTs in the aqueous media. In the spectrum of CuMOF, the absorption peaks at 1446.5 and 729.1 cm^{-1} were assigned to the C═C and C−H bending vibration modes of the benzene rings. Moreover, the peaks at approximately 1368.2, 1588.7, and 1638.7 cm^{-1} were related to the in-plane bonding of C═O bonds.[1] Additionally, the broad peak at 3409.8 cm^{-1} corresponded to the O−H stretching vibrations mode of the intercalated water, and the peak at approximately 488.7 cm^{-1} belonged to the stretching of Cu−O.[29,30] Comparatively speaking, the peaks of CuMOF and CuMOF-SWCNTs@AuNPs were nearly identical. This result potentially occurred because the existence of similar types of groups led to overlapping peaks or the absorption peaks were too weak to appear among the complex due to their low amount of attached loading.

The UV−vis spectra of SWCNT-COOH (curve a), CuMOF (curve b), and CuMOF-SWCNTs@AuNPs (curve c) hybrid are shown in Figure 2B. SWCNT-COOH exhibited high absorption over a wide wavelength range (250−850 nm). The broad peak at around 255 nm was related to the characteristic peak of CuMOF, which is displayed in curve (b).[31] For comparison, as shown in the UV−vis spectra of curve (c), CuMOF-SWCNTs@AuNPs produced a stronger absorption peak near 255 nm with the addition of SWCNTs@AuNPs. Moreover, according to the AuNP-related characteristic absorbance peak at 540 nm (Figure 2B inset), it could be reasonably deduced that the hybrid structure of the CuMOF-SWCNTs@AuNPs was fabricated.

The crystalline structures and crystallinity of the composite materials were confirmed by XRD spectroscopy (Figure 2C). The XRD of SWCNT-COOH presented intense peaks at 2θ = 26.2° and 42.4° marked with diamond, corresponding to the (002) and (101) crystal planes of SWCNTs.[32] In the XRD pattern of CuMOF, the distinct diffraction peaks marked with circles at 2θ = 11.8°, 13.6°, 17.6°, 19.2°, 24.2°, 26.1°, and 29.5° corresponded with the (222), (400), (333), (440), (551), (731), and (751) planes, respectively.[33−35] Nevertheless, several characteristic peaks marked with asterisks assigned to $Cu(OH)_2$ potentially derived from the remaining $Cu(OH)_2$ during its synthesis procedure.[36] In addition, the characteristic peak marked with a square symbol agreed with the (111) surface of CuO.[33,37] The XRD pattern of CuMOF-SWCNTs@AuNPs effectively matched that of CuMOF, and its background appeared as a high-intensity peak at approximately 25°, indicating the coexistence of the SWCNTs. In addition, the composite showed two new diffraction peaks at 2θ values of approximately 38.1 and 44.1° marked with triangles that were attributed to the reflection from the lattice planes of (111) and (200), which closely matched the standard AuNP peaks.[38]

XPS technique was used to investigate the chemical states, valence state, and coordination mode of CuMOF-SWCNT@AuNPs. As the full-scale XPS spectrum displayed in Figure 3A, CuMOF-SWCNTs@AuNPs consisted of C, O, Cu, and Au elements. C 1s XPS spectra (Figure 3B) of the Cu-based nanocomposite showed four peaks at 283.8, 284.8, 286.0, and 288.3 eV that corresponded to C═C, C−C, C−O, and C═O groups, respectively. As shown in Figure 3C, the peak of O 1s was deconvolved into three peaks allocated at 530.1, 531.6, and 533.3 eV, which should be assigned to Cu−O, C═O, and C−O in sequence. For the high-resolution Au 4f XPS spectra of (Figure 3D), the binding energies of Au $4f_{7/2}$ (84.5 eV) and Au $4f_{5/2}$ (88.1 eV) were basically in agreement with the previous literature.[39] Furthermore, Cu in the CuMOF was in the mixed valence state of Cu^{2+}, Cu^{+}, and Cu^{0}. In the high-resolution Cu 2p XPS spectrum (Figure 3E), the scale with a mainly core region at 934.5 and 955.6 eV was sequentially attributed to Cu^{2+} $2p_{3/2}$ and $2p_{1/2}$ along with satellite peaks in CuMOF. In

https://doi.org/10.1021/acsomega.3c08002
ACS Omega 2024, 9, 4744−4753

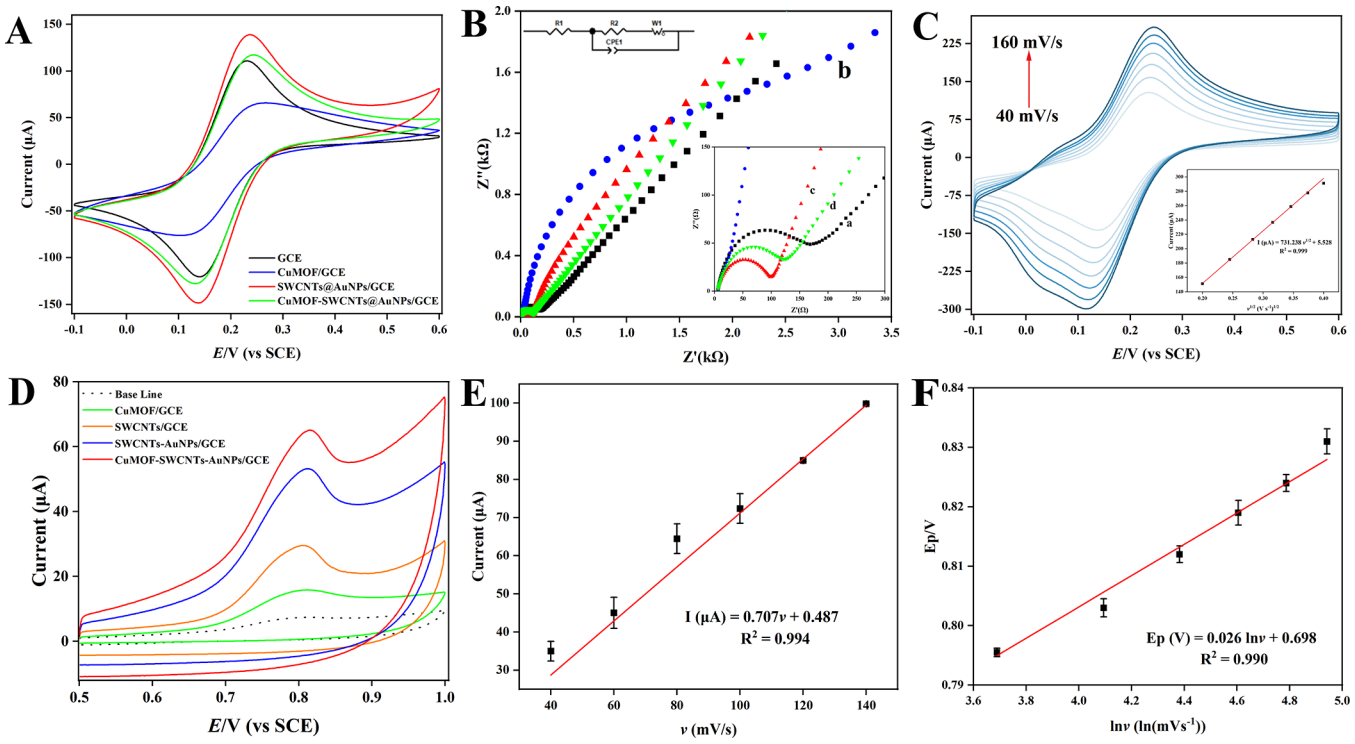

Figure 4. (A) Cyclic voltammograms and (B) Nyquist spectrum of bare GCE (a), CuMOF/GCE (b), SWCNTs@AuNPs/GCE (c), and CuMOF-SWCNTs@AuNPs/GCE (d). (C) Cyclic voltammograms of CuMOF-SWCNTs@AuNPs/GCE at scanning rates from 40 to 160 mV/s in a 5.0 mM $[Fe(CN)_6]^{3-/4-}$ aqueous solution containing 0.1 M KCl (inset shows the plot of I_p vs $\nu^{1/2}$). (D) CV curves of 1.0 μM IMA at different electrodes in phosphate buffer solution (0.1 M, pH = 7.0). (E) Linear calibration plot for peak currents vs scanning rate (40−140 mV/s) in the presence of 3.0 μM IMA. (F) Corresponding plot of E_p and logarithm of ν.

addition, two lower dwarf peaks at 932.6 and 953.7 eV indicated the existence of Cu^0 and Cu^+.[40] Consequently, during the formation reaction of the CuMOF, some of Cu^{2+} was reduced to Cu^+, elucidating the higher activity of CuMOF. The above XPS results demonstrated that CuMOF-SWCNT@AuNP nanocompounds were successfully fabricated.

3.2. Electrochemical Conductivity of CuMOF-SWCNTs@AuNPs/GCE. Cyclic voltammetry (CV) was used for the electrochemical characterization of different modified electrodes in a 5.0 mM $[Fe(CN)_6]^{3-/4-}$ solution including 0.1 M KCl at 50 mV s^{-1} (Figure 4A). Owing to the conductive and catalytic properties of SWCNTs@AuNPs on the sensing platform, more current signals were obtained in the curve of SWCNTs@AuNPs/GCE. Comparatively, due to the blockage effect of CuMOF on electronic transfer, the anodic and anodic peak signals decreased on the bare GCE and SWCNTs@AuNPs/GCE.

After that, electrical impedance spectroscopy (EIS) was also applied to determine stepwise modification of electrodes and describe the electrochemical properties at electrode interfaces. The equivalent circuit diagram fitting the experimental EIS data is displayed in the inset of Figure 4B. As shown in Figure 4B, the Nyquist curve (a) represents the bare electrode without any modification. By dripping the CuMOF on the surface of the GCE (curveb), the electron-transfer resistance (R_{ct}) significantly increased, indicating that CuMOF had poor conductivity. In other words, the process of charge transfer between the surface of CuMOF/GCE and $[Fe(CN)_6]^{3-/4-}$ was decelerated. Moreover, the SWCNT@AuNP nanohybrid decreased the charge-transfer resistance due to the great electron transport capability and excellent conductivity (curvec). However, when the fully modified CuMOF-SWCNTs@AuNPs/GCE (curved) was tested, the impedance curve of the modified electrode was slightly increased compared to that from SWCNTs@AuNPs/GCE. Thus, this result demonstrated that CuMOF was immobilized on the SWCNTs@AuNPs/GCE film. Detailed information regarding R_{ct} is listed in Table S1.

The electrochemically active surface areas of the various modified electrodes were measured through CV at various scanning rates (40−160 mV s^{-1}). The efficacy of the embedded sensors was analyzed according to the Randles−Sevcik eq 1 at 25 °C.[41]

$$I_p = 269,000 n^{3/2} A D^{1/2} C \nu^{1/2} \quad (1)$$

where I_p is the peak current, n is the electron-transfer number in the process (usually n = 1), A is the electrode surface area (cm^2), D is the diffusion coefficient (7.6×10^{-6} cm^2/s), C is the concentration of the redox couple (mol/cm^3), and ν is the scan rating (V/s).[42] From Figure 4C, the slopes from the plot of I_p against $\nu^{1/2}$ were applied for the measurement of the electroactive surface areas, and the A values were calculated as 0.18, 0.03, and 0.21 cm^2 for bare GCE, CuMOF/GCE, and CuMOF-SWCNTs@AuNPs/GCE. Therefore, the sensitivity of CuMOF-SWCNTs@AuNPs/GCE during electroanalysis was reinforced due to its considerable enhancement in its electroactive surface area. Moreover, the EIS performed for all modified electrodes was utilized to calculate the k_{app} constant (eq 2):

$$k_{app} = \frac{R \cdot T}{n^2 \cdot F^2 \cdot A \cdot C \cdot R_{ct}} \quad (2)$$

https://doi.org/10.1021/acsomega.3c08002
ACS Omega 2024, 9, 4744−4753

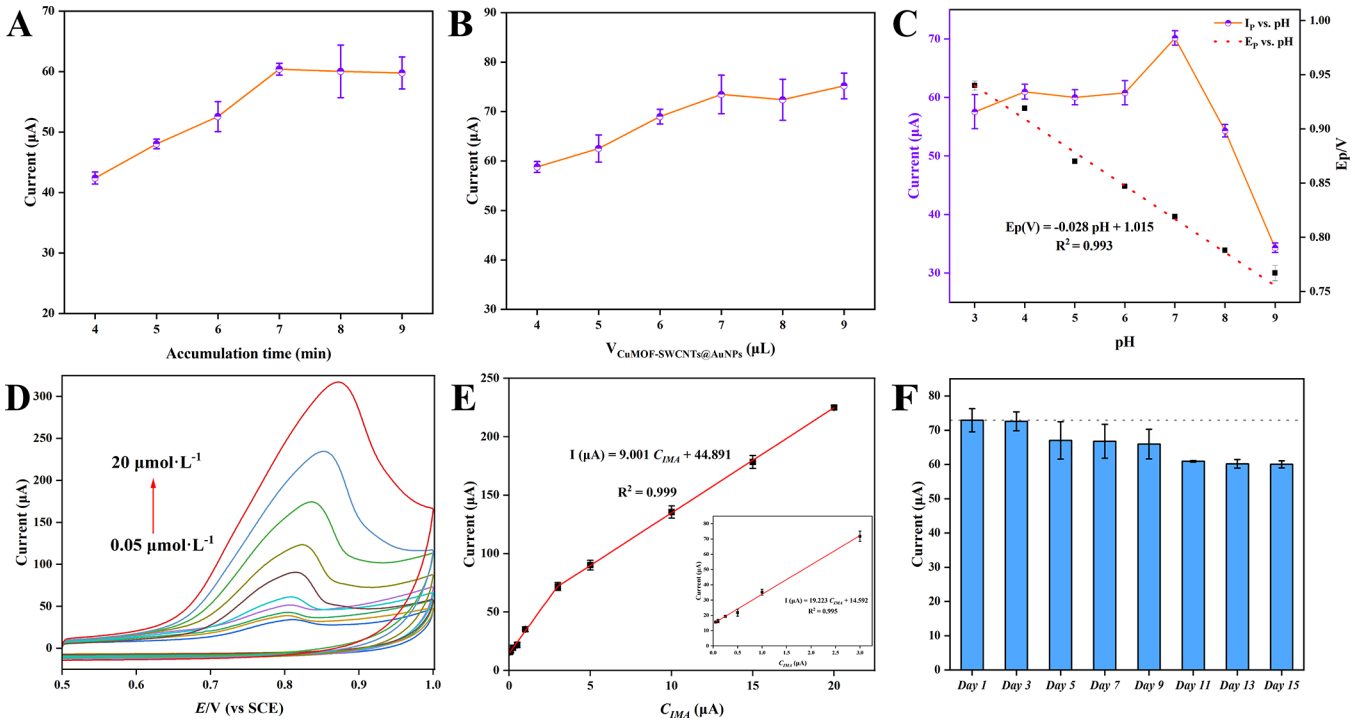

Figure 5. Effect of (A) as the IMA accumulation time and (B) as the dripping amount of CuMOF-SWCNTs@AuNPs. (C) Corresponding plots of E_P vs pH and I_P vs pH. (D) CV curves at CuMOF-SWCNTs@AuNPs/GCE for different IMA concentrations (0.05−20.0 μM) in PBS solution (pH 7.0). (E) Corresponding relationships between I_P and concentrations of IMA. (F) Stability of sensors during the 15-day storage period.

where R, T, F, and A are the same as above, k_{app} is the apparent charge-transfer rate constant (cm/s), n is the number of interchanged electrons (n = 1), C is the bulk concentration of $[Fe(CN)_6]^{3-/4-}$ (5.0 mol cm^3), and R_{ct} is the electron-transfer resistance (Ω). In accordance with the calculation (Table S1), the k_{app} value for CuMOF-SWCNTs@AuNPs/GCE was almost 1.1- and 2.9-fold greater than those for the bare GCE and CuMOF/GCE. This observation indicated that the charge-transfer process was much easier at the CuMOF-SWCNTs@AuNPs/GCE compared to that at the other prepared electrodes. In addition, Figure S1 displays the experimental and fitting impedance spectra of CuMOF-SWCNTs@AuNPs/GCE; a similar consistency between the experimental and fitted data was observed.

3.3. Electrocatalytic Behaviors and Mechanism of IMA on CuMOF-SWCNTs@AuNPs/GCE. As a pyridinium compound, IMA can chelate with the open metal sites of the CuMOF;[43] after adsorbing IMA on the surface of modified electrodes, an electro-oxidation reaction of this drug occurs. The electrocatalytic behavior of CuMOF-SWCNTs@AuNPs/GCE toward IMA (1.0 μM) was investigated in PBS solution (pH 7) using the *CV* technique. As shown in Figure 4D, all of the modified electrodes exhibited only one oxidation peak at approximately +0.81 V; however, no relevant reduction peak was perceived in the reverse scan. This observation showed that the IMA oxidation reaction was an irreversible and surface-controlled process.

The signal on the CuMOF/GCE (7.98 μA) was quite weak, with a broad anodic peak; thus, the IMA direct charge-transfer rate was slower on its surface due to its poor electrical conductivity. Instead, SWCNTs and AuNPs with superiorly conductive and catalytic properties could promote charge transfer. Moreover, CuMOF also adsorbs IMA as a guest in the surface cavity and accumulates it due to its porosity. Simultaneously, CuMOF has Lewis acid coordination sites on its interior pore wall, so the Cu sites are feasible for electrocatalytic conversions.[35] Compared with the single SWCNTs (21.82 μA) and SWCNTs@AuNPs (31.13 μA), CuMOF-SWCNTs@AuNPs/GCE showed an apparent enhancement in the current signal by 26.77 and 9.79%, which clearly demonstrated the electrocatalytic activity of CuMOF-SWCNTs@AuNPs for IMA electrooxidation.

To study the redox mechanisms of IMA on CuMOF-SWCNTs@AuNPs/GCE, the effect of scanning rates from 40 to 140 mV s^{-1} was investigated. Figure S2 shows the cyclic voltammograms at CuMOF-SWCNTs@AuNPs/GCE in a 3.0 μM IMA solution for various scanning rates; an irreversible oxidation peak was observed in the forward potential scanning. Moreover, the oxidation peak potential (E_P) positively shifted as the scan rate increased. In Figure 4E, the peak currents linearly increased with the scanning rate (R^2=0.994); this result also confirmed that the oxidation process of IMA was a surface-controlled process. Meanwhile, the linearity between E_P and lnυ based on Laviron's eq 3 is defined as follows:

$$E_P = E^0 + [RT/(1-\alpha)nF]\ln[RTk_s/(1-\alpha)nF] + [RT/(1-\alpha)nF]\ln\upsilon \quad (3)$$

where R, T, and F are constant numbers and E^0, n, k_s, υ, and α are the standard redox potential, the number of transferred electrons, the rate constant of the electrochemical reaction, the various scanning rates, and the charge-transfer coefficient, respectively. Through the slope (0.026) of E_P vs ln υ (Figure 4F), the value of $(1-\alpha)$ n was calculated as 0.99. In addition, α and n were usually identified as 0.5 and 1.0 in the irreversible redox reaction. Thus, two electrons participated in the oxidation reaction of IMA at CuMOF-SWCNTs@AuNPs/GCE.

https://doi.org/10.1021/acsomega.3c08002
ACS Omega 2024, 9, 4744−4753

Scheme 2. Possible Electro-Oxidation Mechanism of IMA on the Surface of CuMOF-SWCNTs@AuNPs/GCE

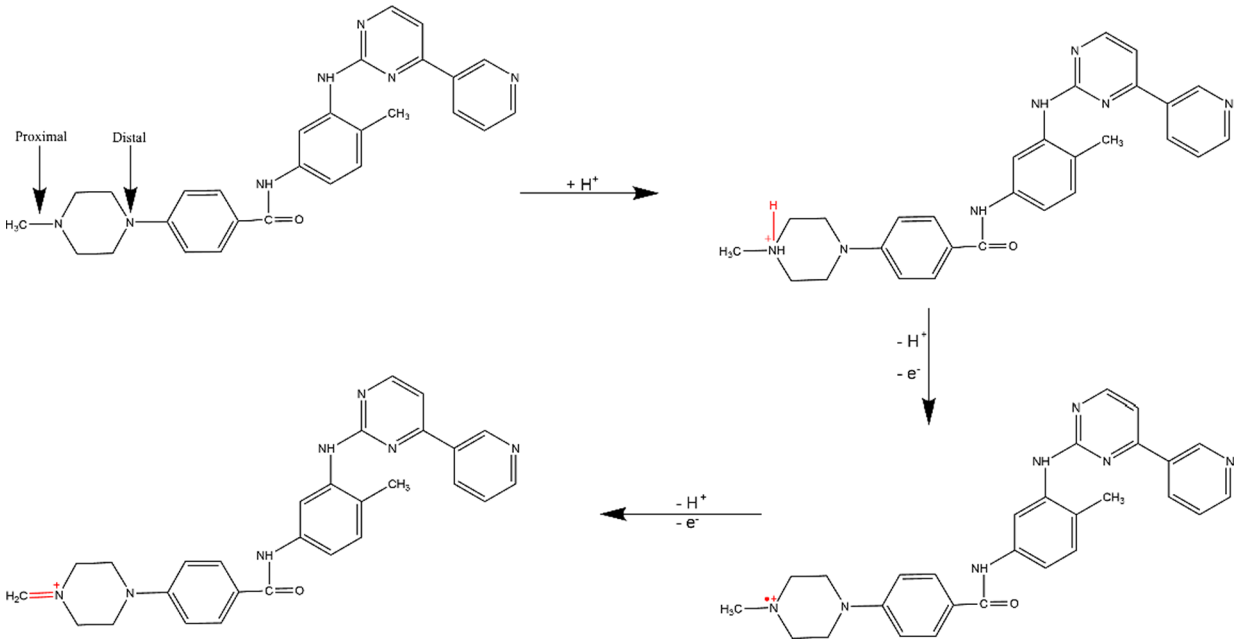

3.4. Optimization of the Experimental Variables. To determine the best performance of this prepared sensor, a series of parameters, including IMA accumulation time, the amount of CuMOF-SWCNTs@AuNPs, and the pH values of PBS, were investigated. Figure 5A displays the effect of accumulation time (t_{ac}) on the oxidation peak current of IMA. As accumulation time was prolonged, the current response of IMA remarkably increased. However, when the accumulation time was longer than 7 min, the current signal response of IMA reached an equilibrium state, indicating that the adsorption process was primarily completed after 7 min and that the adsorption of IMA reached saturation on the surface of the fabricated electrode. Therefore, 7 min was selected as the optimum accumulation time. In addition, six different amounts of modified materials from 4 to 9 μL were compared with their current response to determine the best condition (Figure 5B). The anodic peak signal of IMA initially improved as the amount of CuMOF-SWCNTs@AuNPs increased from 4 to 7 and tended to gradually stabilize when the amount was greater than 7 μL. This result could be attributed to the fact that the electrode surface was not totally covered when the dropping amount was less than 7 μL. Consequently, the optimal amount of CuMOF-SWCNTs@AuNPs was selected as 7 μL.

As the electrode reaction process is usually influenced by protons, the pH value of PBS also plays a critical role in IMA detection. To obtain the optimum pH for IMA oxidation using CuMOF-SWCNTs@AuNPs/GCE as the modified electrode, the influence of the pH value on the anodic peak current (I_P) was investigated (Figure 5C). By increasing the pH over the range of 3 to 9, the I_P signal of IMA gradually increased. Notably, when the pH exceeded 7, the I_P value decreased. This phenomenon was potentially attributed to the three pK_a values of IMA (pK_{a1} = 2.5, pK_{a2} = 4.0, and pK_{a3} = 8.2).[44] When the solution pH was 7.0, the IMA surface was positively charged, while it was negatively charged at pH > 8.2. In addition, with CuMOF as an adsorbent, its surface was negatively charged when pH > 4; thus, the highest current was obtained at pH of 7 owing to the electrostatic attraction of the different polarity charges. Thus, pH 7 was chosen as the optimal value for the following experiments.

In addition, the CV curves of the fabricated electrodes in the presence of 3.0 μM IMA at different pH values are shown in Figure S3. Apparently, the E_P of IMA shifted toward less positive potentials when the pH increased; this result confirmed that protons participated in the electrochemical reaction of IMA. Moreover, the linear regression equation of E_P versus pH (Figure 5C) was achieved as E_P = −0.028 pH + 1.015 (R^2 = 0.993), and the obtained slope value (0.028 V) was approximately half of the theoretical value (0.059 V) of the Nernst equation, indicating that one proton (H^+) and two electrons (e^-) participated in the redox reaction. The results were consistent with those discussed in Section 3.3. According to other reports,[14,36] the oxidation process of IMA occurred on the terminal nitrogen atom of the piperazine ring, and the proposed mechanism was comparable to the oxidation of piperazine derivatives; thus, a possible reaction pathway was proposed, as illustrated in Scheme 2.

3.5. Analytical Characteristics of the Sensor. The electrochemical sensor adsorbed different concentrations of IMA in PBS (pH 7) solution for 7 min, with the CV curves recorded in the range of 0.5−1.0 V. The voltammograms are indicated in Figure 5D, and the variation in the I_P as a function of the IMA concentration was achieved as follows (Figure 5E): I (μA) = 19.223C_{IMA} + 14.592 (R^2 = 0.995, 0.05−3.0 μM) and I (μA) = 9.001C_{IMA} + 44.891 (R^2 = 0.999, 3.0−20.0 μM). This result was potentially attributed to forming the IMA monolayer coverage on the surface of the electrode at lower concentrations; in contrast, multilayers covered the modified electrodes at higher concentrations. In addition, the limit of detection (LOD) was obtained by eq 4 as follows:

$$\mathrm{LOD} = \frac{3\sigma\mathrm{blank}}{m} \tag{4}$$

where σ_{blank} is the standard deviation of the blank signal and m is the slope; thus, the LOD (S/N = 3) of the as-produced electrode was estimated to be 5.2 nM for IMA. The CuMOF-

https://doi.org/10.1021/acsomega.3c08002
ACS Omega 2024, 9, 4744−4753

SWCNTs@AuNPs composite material provided an enhanced analytical characteristic for IMA detection in terms of a lower LOD and wider linear range than those of previously already reported methods (summarized in Table S2). Our developed method easily and rapidly prepared the samples, which were added dropwise to the CuMOF-SWCNTs@AuNPs to form the dispersion on the electrode surface; this process was performed without a complicated process or tedious sample preparation. The applicability of forming a composite-film-based CuMOF on the electrode surfaces for the simple construction of the electrochemical sensors was demonstrated.

To demonstrate the selectivity of this fabricated sensor in therapeutic drug monitoring, our proposed approach was used to identify IMA from other conventional interferents, including organics (such as glucose, citric acid, dopamine, uric acid, glycine, L-cysteine, and ascorbic acid) and inorganic ions (such as K^+, Na^+, Ca^{2+}, Zn^{2+}, Mg^{2+}, Fe^{3+}, Fe^{2+}, Cl^-, and SO_4^{2-}). The detailed results (summarized in Table 1) showed that there was no apparent interference, indicating that these investigated compounds had minimal influence on IMA detection.

Table 1. Interference Effects of Various Substances for 3.0 μM IMA

interference	tolerance level
K^+, Na^+, Ca^{2+}, Zn^{2+}, Mg^{2+}, Fe^{3+}, Cl^-	1000
dopamine	400
glucose, uric acid, ascorbic acid	250
glycine, L-cysteine	200
citric acid	150
Fe^{2+}, SO_4^{2-}	50

To evaluate the repeatability and reproducibility of our prepared sensor. Five electrodes were applied for the determination of 1.5 μM IMA, and a relative standard deviation (RSD) value of 7.3% showed accessible reproducibility of the sensor for IMA determination. Furthermore, our sensor was separately prepared five times with the same GCE. IMA (1.5 μM) was tested, and the RSD of the measurements was 7.6%, which indicated the excellent reproducibility of the sensor. The stability of the proposed sensor was estimated by detecting 1.5 μM IMA after it was stored in a 4 °C freezer. After 15 consecutive days of storage (Figure 5F), the current signal of the sensor reached 82.3% compared to the initial detection. These results showed acceptable selectivity, repeatability, reproducibility, and storage stability of our developed strategy.

3.6. Imatinib Analysis in Practical Samples. To assess the feasibility of the electrochemical sensor, the recovery of different concentrations of IMA standards in healthy serum samples was used to analyze the accuracy of this method. From Table S3, each sample was evaluated in triplicate with recoveries ranging from 92.48 to 105.68%, and the RSD was obtained to be less than 10.39% (n = 3). In addition, HPLC has long been the main method used for therapeutic drug monitoring; thus, several different IMA concentrations from patient serum samples were detected by using CV and HPLC−MS (Table 2). The recoveries of the patient's serum samples were in the range of 97.21−106.21%, with the highest RSD of 8.0%. Hence, the testing results from both methods were consistent, indicating that our proposed analysis procedure could be efficiently used for the selective detection of IMA in human serum without biological effect.

Table 2. Recovery of IMA in Human Serum Samples (n = 3)

sample	HPLC−MS method found (μM)	CV method found (μM)	recovery (%)	RSD
1	1.2196	1.1998	98.38	0.0110
2	1.4485	1.4081	97.21	0.0804
3	1.8031	1.9150	106.21	0.0554
4	2.2893	2.2539	98.45	0.0266
5	2.9781	3.0748	103.25	0.0357
6	4.0727	4.0118	98.52	0.0215

4. CONCLUSIONS

Conclusively, this study describes an approach for the electrocatalytic detection of IMA with the synergistic effects of CuMOF and SWCNT@AuNP nanostructures. With the superior conductivity of SWCNTs@AuNPs and the adsorption of CuMOFs, our proposed modified-GCE validated the attainable selectivity, reproducibility, repeatability, and long-term stability. In addition, this method was successfully applied to the detection of IMA in spiked blood serum and clinical patient blood serum with a satisfactory recovery rate. Furthermore, our novel electrochemical sensor could be a practical nanoplatform tool for IMA detection, showing its potential application in therapeutic drug monitoring.

■ ASSOCIATED CONTENT

Supporting Information

The Supporting Information is available free of charge at https://pubs.acs.org/doi/10.1021/acsomega.3c08002.

Chemicals, reagents and apparatus, synthesis processes of materials, fabrication of modified GCE, processing procedures and detection of the IMA sample, experimental and simulated Nyquist plots for CuMOF-SWCNTs@AuNPs/GCE, electrochemical behavior of the prepared sensor at different scan rates and different pH, parameters of the equivalent circuit components for modified electrodes, various sensor performances for IMA determination, and recovery of the fabricated sensor in real clinical samples (PDF)

■ AUTHOR INFORMATION

Corresponding Author

Deng Pan − *Department of Clinical Laboratory, The Affiliated Hospital of Qingdao University, Qingdao, Shandong 266000, China*; orcid.org/0000-0002-9293-3566; Email: pandenglaoshi@163.com

Authors

Xuanming Xu − *Department of Clinical Laboratory, The Affiliated Hospital of Qingdao University, Qingdao, Shandong 266000, China*

Wei Li − *Clinical Laboratory, Qingdao Women and Children's Hospital Affiliated, Qingdao University, Qingdao 266034, China*

Hao Xin − *Department of Clinical Laboratory, The Affiliated Hospital of Qingdao University, Qingdao, Shandong 266000, China*

Lian Tang − *Department of Neurology, Qingdao Municipal Hospital, Qingdao University, Qingdao 266000, China*

Xiaoyan Zhou − *Department of Clinical Laboratory, The Affiliated Hospital of Qingdao University, Qingdao,*

https://doi.org/10.1021/acsomega.3c08002
ACS Omega 2024, 9, 4744−4753

Shandong 266000, China; orcid.org/0000-0002-8289-1139

Tingting Zhou − *Department of Clinical Laboratory, The Affiliated Hospital of Qingdao University, Qingdao, Shandong 266000, China*

Chao Xuan − *Department of Clinical Laboratory, The Affiliated Hospital of Qingdao University, Qingdao, Shandong 266000, China*

Qingwu Tian − *Department of Clinical Laboratory, The Affiliated Hospital of Qingdao University, Qingdao, Shandong 266000, China*

Complete contact information is available at: https://pubs.acs.org/10.1021/acsomega.3c08002

Author Contributions

X.X. and W.L.: Investigation, writing-original draft. H.X. and L.T.: Investigation, methodology, writing-review, and editing. X.Z., C.X., and T.Z.: Writing-review and editing. Q.T.: Investigation and formal analysis. D.P.: Review, supervision, and funding acquisition. X.X. and W.L. contributed equally to this work.

Notes

The authors declare no competing financial interest.

■ ACKNOWLEDGMENTS

This work was supported by the National Natural Science Foundation of China (82204099), the Natural Science Foundation of Shandong Province, China (ZR202102200297), the Clinical Medicine + X Scientific Research of the Affiliated Hospital of Qingdao University, China (QDFY+X2021062), the Qingdao Postdoctoral Applied Research Project, and the China Postdoctoral Science Foundation (2022M721755).

■ REFERENCES

(1) Kantarjian, H.; Sawyers, C.; Hochhaus, A.; Guilhot, F.; Schiffer, C.; Gambacorti-Passerini, C.; Niederwieser, D.; Resta, D.; Capdeville, R.; Zoellner, U.; et al. Hematologic and Cytogenetic Responses to Imatinib Mesylate in Chronic Myelogenous Leukemia. *New Engl. J. Med.* **2002**, *346* (9), 645−652.

(2) Druker, B. J.; Sawyers, C. L.; Kantarjian, H.; Resta, D. J.; Reese, S. F.; Ford, J. M.; Capdeville, R.; Talpaz, M. Activity of a Specific Inhibitor of the BCR-ABL Tyrosine Kinase in the Blast Crisis of Chronic Myeloid Leukemia and Acute Lymphoblastic Leukemia with the Philadelphia Chromosome. *New Engl. J. Med.* **2001**, *344* (14), 1038−1042.

(3) Gajski, G.; Gerić, M.; Domijan, A.-M.; Golubović, I.; Garaj-Vrhovac, V. Evaluation of oxidative stress responses in human circulating blood cells after imatinib mesylate treatment − Implications to its mechanism of action. *Saudi Pharmaceutical Journal* **2019**, *27* (8), 1216−1221.

(4) Guilhot, F.; Hughes, T. P.; Cortes, J.; Druker, B. J.; Baccarani, M.; Gathmann, I.; Hayes, M.; Granvil, C.; Wang, Y. Plasma exposure of imatinib and its correlation with clinical response in the Tyrosine Kinase Inhibitor Optimization and Selectivity Trial. *Haematologica* **2012**, *97* (5), 731−738.

(5) Larson, R. A.; Druker, B. J.; Guilhot, F.; O'Brien, S. G.; Riviere, G. J.; Krahnke, T.; Gathmann, I.; Wang, Y. Imatinib pharmacokinetics and its correlation with response and safety in chronic-phase chronic myeloid leukemia: a subanalysis of the IRIS study. *Blood* **2008**, *111* (8), 4022−4028.

(6) Yang, J. S.; Cho, E. G.; Huh, W.; Ko, J.-W.; Jung, J. A.; Lee, S.-Y. Rapid determination of imatinib in human plasma by liquid chromatography-tandem mass spectrometry: application to a pharmacokinetic study. *Korean Chem. Soc.* **2013**, *34* (8), 2425−2430.

(7) Roth, O.; Spreux-Varoquaux, O.; Bouchet, S.; Rousselot, P.; Castaigne, S.; Rigaudeau, S.; Raggueneau, V.; Therond, P.; Devillier, P.; Molimard, M.; et al. Imatinib assay by HPLC with photodiode-array UV detection in plasma from patients with chronic myeloid leukemia: Comparison with LC-MS/MS. *Clin. Chim. Acta* **2010**, *411* (3), 140−146.

(8) Ajithkumar, P.; Smith, A. J. D. Development of analytical method for imatinib mesylate by ultraviolet spectroscopy. *Asian J. Pharm. Clin. Res.* **2020**, *13* (1), 180.

(9) Fornasaro, S.; Bonifacio, A.; Marangon, E.; Buzzo, M.; Toffoli, G.; Rindzevicius, T.; Schmidt, M. S.; Sergo, V. Label-Free Quantification of Anticancer Drug Imatinib in Human Plasma with Surface Enhanced Raman Spectroscopy. *Anal. Chem.* **2018**, *90* (21), 12670−12677.

(10) Yan, Z.; Zhang, Z.; Chen, J. Biomass-based carbon dots: Synthesis and application in imatinib determination. *Sens. Actuators, B* **2016**, *225*, 469−473.

(11) Lahcen, A. A.; Rauf, S.; Beduk, T.; Durmus, C.; Aljedaibi, A.; Timur, S.; Alshareef, H. N.; Amine, A.; Wolfbeis, O. S.; Salama, K. N. Electrochemical sensors and biosensors using laser-derived graphene: A comprehensive review. *Biosens. Bioelectron.* **2020**, *168*, No. 112565.

(12) Sun, J.; Wang, Z.; Guan, J. Single-atom nanozyme-based electrochemical sensors for health and food safety monitoring. *Food Chem.* **2023**, *425*, No. 136518.

(13) Alvau, M. D.; Tartaggia, S.; Meneghello, A.; Casetta, B.; Calia, G.; Serra, P. A.; Polo, F.; Toffoli, G. Enzyme-Based Electrochemical Biosensor for Therapeutic Drug Monitoring of Anticancer Drug Irinotecan. *Anal. Chem.* **2018**, *90* (10), 6012−6019.

(14) Ghapanvari, M.; Madrakian, T.; Afkhami, A.; Ghoorchian, A. A modified carbon paste electrode based on Fe3O4@multi-walled carbon nanotubes@polyacrylonitrile nanofibers for determination of imatinib anticancer drug. *J. Appl. Electrochem.* **2020**, *50* (2), 281−294.

(15) Alamgholiloo, H.; Zhang, S.; Ahadi, A.; Rostamnia, S.; Banaei, R.; Li, Z.; Liu, X.; Shokouhimehr, M. Synthesis of bimetallic 4-PySI-Pd@Cu(BDC) via open metal site Cu-MOF: Effect of metal and support of Pd@Cu-MOFs in H2 generation from formic acid. *Molecular Catalysis* **2019**, *467*, 30−37.

(16) Zhou, J.; Li, X.; Yang, L.; Yan, S.; Wang, M.; Cheng, D.; Chen, Q.; Dong, Y.; Liu, P.; Cai, W.; et al. The Cu-MOF-199/single-walled carbon nanotubes modified electrode for simultaneous determination of hydroquinone and catechol with extended linear ranges and lower detection limits. *Anal. Chim. Acta* **2015**, *899*, 57−65.

(17) Abbasi, A. R.; Rizvandi, M.; Azadbakht, A.; Rostamnia, S. Controlled uptake and release of imatinib from ultrasound nanoparticles Cu3(BTC)2 metal−organic framework in comparison with bulk structure. *J. Colloid Interface Sci.* **2016**, *471*, 112−117.

(18) Liu, W.; Yin, X.-B. Metal−organic frameworks for electrochemical applications. *TrAC Trends in Analytical Chemistry* **2016**, *75*, 86−96.

(19) Amatatongchai, M.; Sroysee, W.; Chairam, S.; Nacapricha, D. Simple flow injection for determination of sulfite by amperometric detection using glassy carbon electrode modified with carbon nanotubes−PDDA−gold nanoparticles. *Talanta* **2015**, *133*, 134−141.

(20) Mo, F.; Xie, J.; Wu, T.; Liu, M.; Zhang, Y.; Yao, S. A sensitive electrochemical sensor for bisphenol A on the basis of the AuPd incorporated carboxylic multi-walled carbon nanotubes. *Food Chem.* **2019**, *292*, 253−259.

(21) Mohammadi, A.; Heydari-Bafrooei, E.; Foroughi, M. M.; Mohammadi, M. Heterostructured Au/MoS2-MWCNT nanoflowers: A highly efficient support for the electrochemical aptasensing of solvated mercuric ion. *Microchemical Journal* **2020**, *158*, No. 105154.

(22) Wang, Z.; Dai, Z. Carbon nanomaterial-based electrochemical biosensors: an overview. *Nanoscale* **2015**, *7* (15), 6420−6431.

(23) Lin, Y.; Li, L.; Hu, L.; Liu, K.; Xu, Y. Multifunctional poly(dopamine)-assisted synthesis of silver nano particles/carbon nanotubes nanocomposite: Toward electrochemical sensing of hydrogen peroxide with enhanced sensitivity. *Sens. Actuators, B* **2014**, *202*, 527−535.

(24) Zhao, Z.; Sun, Y.; Li, P.; Zhang, W.; Lian, K.; Hu, J.; Chen, Y. Preparation and characterization of AuNPs/CNTs-ErGO electrochemical sensors for highly sensitive detection of hydrazine. *Talanta* **2016**, *158*, 283−291.
(25) Wang, L.; Liu, Y.; Chen, Y. Effective Electrochemical Sensor Based on Au Nanoparticles Decorated Carboxylated Multi-wall Carbon Nanotube (AuNPS@c-MWCNTs) Nanocomposites for Determination of Dicapthon Pesticide in Agricultural Food. *Int. J. Electrochem. Sci.* **2021**, *16* (4), No. 210464.
(26) Yu, Y.; Chen, Z.; He, S.; Zhang, B.; Li, X.; Yao, M. Direct electron transfer of glucose oxidase and biosensing for glucose based on PDDA-capped gold nanoparticle modified graphene/multi-walled carbon nanotubes electrode. *Biosens. Bioelectron.* **2014**, *52*, 147−152.
(27) Landi, B. J.; Castro, S. L.; Ruf, H. J.; Evans, C. M.; Bailey, S. G.; Raffaelle, R. P. CdSe quantum dot-single wall carbon nanotube complexes for polymeric solar cells. *Sol. Energy Mater. Sol. Cells* **2005**, *87* (1), 733−746.
(28) Gao, G.; Pan, M.; Vecitis, C. D. J. J. Effect of the oxidation approach on carbon nanotube surface functional groups and electrooxidative filtration performance. *Journal of Materials Chemistry A* **2015**, *3* (14), 7575−7582.
(29) Wang, F.; Guo, H.; Chai, Y.; Li, Y.; Liu, C. The controlled regulation of morphology and size of HKUST-1 by "coordination modulation method. *Microporous Mesoporous Mater.* **2013**, *173*, 181−188.
(30) Wang, Q.; Yang, Y.; Gao, F.; Ni, J.; Zhang, Y.; Lin, Z. Graphene Oxide Directed One-Step Synthesis of Flowerlike Graphene@HKUST-1 for Enzyme-Free Detection of Hydrogen Peroxide in Biological Samples. *ACS Appl. Mater. Interfaces* **2016**, *8* (47), 32477−32487.
(31) Gao, Y.; Zhou, D.; Xu, Q.; Li, J.; Luo, W.; Yang, J.; Pan, Y.; Huang, T.; Wang, Y.; He, B.; et al. Metal−Organic Framework-Mediated Bioorthogonal Reaction to Immobilize Bacteria for Ultrasensitive Fluorescence Counting Immunoassays. *ACS Appl. Mater. Interfaces* **2023**, *15* (4), 5010−5018.
(32) Cao, A.; Xu, C.; Liang, J.; Wu, D.; Wei, B. X-ray diffraction characterization on the alignment degree of carbon nanotubes. *Chem. Phys. Lett.* **2001**, *344* (1), 13−17.
(33) Okada, K.; Ricco, R.; Tokudome, Y.; Styles, M. J.; Hill, A. J.; Takahashi, M.; Falcaro, P. Copper Conversion into Cu(OH)2 Nanotubes for Positioning Cu3(BTC)2 MOF Crystals: Controlling the Growth on Flat Plates, 3D Architectures, and as Patterns. *Adv. Funct. Mater.* **2014**, *24* (14), 1969−1977.
(34) Shahrokhian, S.; Khaki Sanati, E.; Hosseini, H. Direct growth of metal-organic frameworks thin film arrays on glassy carbon electrode based on rapid conversion step mediated by copper clusters and hydroxide nanotubes for fabrication of a high performance non-enzymatic glucose sensing platform. *Biosens. Bioelectron.* **2018**, *112*, 100−107.
(35) Schlichte, K.; Kratzke, T.; Kaskel, S. Improved synthesis, thermal stability and catalytic properties of the metal-organic framework compound Cu3(BTC)2. *Microporous Mesoporous Mater.* **2004**, *73* (1), 81−88.
(36) Rezvani Jalal, N.; Madrakian, T.; Afkhami, A.; Ghoorchian, A. In Situ Growth of Metal−Organic Framework HKUST-1 on Graphene Oxide Nanoribbons with High Electrochemical Sensing Performance in Imatinib Determination. *ACS Appl. Mater. Interfaces* **2020**, *12* (4), 4859−4869.
(37) Tan, J.; Dun, M.; Li, L.; Zhao, J.; Li, X.; Hu, Y.; Huang, G.; Tan, W.; Huang, X. Self-template derived CuO nanowires assembled microspheres and its gas sensing properties. *Sens. Actuators, B* **2017**, *252*, 1−8.
(38) Khatua, A.; Priyadarshini, E.; Rajamani, P.; Patel, A.; Kumar, J.; Naik, A.; Saravanan, M.; Barabadi, H.; Prasad, A.; Gosh, I.; et al. Phytosynthesis, Characterization and Fungicidal Potential of Emerging Gold Nanoparticles Using Pongamia pinnata Leave Extract: A Novel Approach in Nanoparticle Synthesis. *J. Cluster Sci.* **2020**, *31* (1), 125−131.
(39) Rakočević, L.; Štrbac, S.; Srejić, I. Hydrogen evolution on Au/GC and PdAu/GC nanostructures in acid solution: AFM, XPS, and electrochemical study. *Int. J. Hydrogen Energy* **2021**, *46* (13), 9052−9063.
(40) Ghodselahi, T.; Vesaghi, M. A.; Shafiekhani, A.; Baghizadeh, A.; Lameii, M. XPS study of the Cu@Cu2O core-shell nanoparticles. *Appl. Surf. Sci.* **2008**, *255* (5), 2730−2734.
(41) Foroughi, M. M.; Jahani, S.; Aramesh-Boroujeni, Z.; Vakili Fathabadi, M.; Hashemipour Rafsanjani, H.; Rostaminasab Dolatabad, M. Template-free synthesis of ZnO/Fe3O4/Carbon magnetic nanocomposite: Nanotubes with hexagonal cross sections and their electrocatalytic property for simultaneous determination of oxymorphone and heroin. *Microchemical Journal* **2021**, *170*, No. 106679.
(42) Taherizadeh, M.; Jahani, S.; Moradalizadeh, M.; Foroughi, M. M. Synthesis of a dual-functional terbium doped copper oxide nanoflowers for high-efficiently electrochemical sensing of ofloxacin, pefloxacin and gatifloxacin. *Talanta* **2023**, *255*, No. 124216.
(43) Qi, C.; Cai, Q.; Zhao, P.; Jia, X.; Lu, N.; He, L.; Hou, X. The metal-organic framework MIL-101(Cr) as efficient adsorbent in a vortex-assisted dispersive solid-phase extraction of imatinib mesylate in rat plasma coupled with ultra-performance liquid chromatography/mass spectrometry: Application to a pharmacokinetic study. *Journal of Chromatography A* **2016**, *1449*, 30−38.
(44) Mioduszewska, K.; Dołżonek, J.; Wyrzykowski, D.; Kubik, Ł.; Wiczling, P.; Sikorska, C.; Toński, M.; Kaczyński, Z.; Stepnowski, P.; Białk-Bielińska, A. Overview of experimental and computational methods for the determination of the pKa values of 5-fluorouracil, cyclophosphamide, ifosfamide, imatinib and methotrexate. *TrAC Trends in Analytical Chemistry* **2017**, *97*, 283−296.

https://doi.org/10.1021/acsomega.3c08002
ACS Omega 2024, 9, 4744−4753